European Journal of Nuclear Medicine and Molecular Imaging (2019) 46:1952–1965
https://doi.org/10.1007/s00259-019-04357-w

ORIGINAL ARTICLE

Synthesis and in vivo evaluation of [^{18}F]UCB-J for PET imaging of synaptic vesicle glycoprotein 2A (SV2A)

Songye Li[1] · Zhengxin Cai[1] · Wenjie Zhang[2] · Daniel Holden[1] · Shu-fei Lin[1] · Sjoerd J. Finnema[1] · Anupama Shirali[1] · Jim Ropchan[1] · Stephane Carre[3] · Joel Mercier[3] · Richard E. Carson[1] · Nabeel Nabulsi[1] · Yiyun Huang[1]

Received: 25 January 2019 / Accepted: 2 May 2019 / Published online: 7 June 2019

Abstract

Purpose Synaptic abnormalities have been implicated in a variety of neuropsychiatric disorders, including epilepsy, Alzheimer's disease, and schizophrenia. Hence, PET imaging of the synaptic vesicle glycoprotein 2A (SV2A) may be a valuable in vivo biomarker for neurologic and psychiatric diseases. We previously developed [^{11}C]UCB-J, a PET radiotracer with high affinity and selectivity toward SV2A; however, the short radioactive half-life (20 min for ^{11}C) places some limitations on its broader application. Herein, we report the first synthesis of the longer-lived ^{18}F-labeled counterpart (half-life: 110 min), [^{18}F]UCB-J, and its evaluation in nonhuman primates.

Methods [^{18}F]UCB-J was synthesized from the iodonium precursors. PET imaging experiments with [^{18}F]UCB-J were conducted in rhesus monkeys to assess the pharmacokinetic and in vivo binding properties. Arterial samples were taken for analysis of radioactive metabolites and generation of input functions. Regional time–activity curves were analyzed using the one-tissue compartment model to derive regional distribution volumes and binding potentials for comparison with [^{11}C]UCB-J.

Results [^{18}F]UCB-J was prepared in high radiochemical and enantiomeric purity, but low radiochemical yield. Evaluation in nonhuman primates indicated that the radiotracer displayed pharmacokinetic and imaging characteristics similar to those of [^{11}C]UCB-J, with moderate metabolism rate, high brain uptake, fast and reversible binding kinetics, and high specific binding signals.

Conclusion We have accomplished the first synthesis of the novel SV2A radiotracer [^{18}F]UCB-J. [^{18}F]UCB-J is demonstrated to be an excellent imaging agent and may prove to be useful for imaging and quantification of SV2A expression, and synaptic density, in humans.

Keywords SV2A · PET · Radiotracer · Fluorination · Nonhuman primates · Alzheimer's disease

Introduction

The synaptic vesicle glycoprotein 2A (SV2A) is one of the three isoforms of synaptic vesicle glycoprotein 2 (SV2), and is expressed ubiquitously in all neurons across the brain [1, 2]. As a vesicle protein, SV2A is essential for neural function and can be used as a biomarker of synaptic density [3, 4]. Further, changes in SV2A have been implicated in a variety of neurologic and psychiatric disorders, including epilepsy [1, 5, 6], Alzheimer's disease (AD) [7, 8], Parkinson's disease (PD) [9], and schizophrenia [10]. For example, regional synaptic loss has been shown to be a robust indicator of neurodegeneration [11]. As a result, its measurement can potentially serve as a diagnostic or prognostic tool for AD and other neurodegenerative diseases, and thus may allow the early detection of these diseases at the preclinical or prodromal stage [12]. Positron

Songye Li and Zhengxin Cai contributed equally to this work.

This article is part of the Topical Collection on Translational Research

✉ Songye Li
songye.li@yale.edu

✉ Zhengxin Cai
jason.cai@yale.edu

[1] PET Center, Department of Radiology and Biomedical Imaging, Yale University, New Haven, CT 06520, USA

[2] Department of Nuclear Medicine, West China Hospital of Sichuan University, Chengdu 610041, Sichuan, China

[3] UCB Biopharma, Braine-l'Alleud, Belgium

emission tomography (PET) is a noninvasive and quantitative imaging technique used to investigate physiological and biochemical changes in living subjects. Hence, the development and application of SV2A PET imaging agents can facilitate the investigation and understanding of the structural disruption and alterations of synapses in diseases, and in the evaluation of drug candidates targeted at synaptic repair and restoration.

Within the past few years, we have prepared three radiotracers, [^{11}C]UCB-A (**1**), [^{18}F]UCB-H (**2**), and [^{11}C]UCB-J (**3**), and evaluated their ability to image and quantify SV2A in vivo (Fig. 1). Among these three ligands, [^{11}C]UCB-A suffers from slow kinetics [13] and [^{18}F]UCB-H provides limited specific binding signals in monkeys and humans [14–17]. Replacement of the fluorine substituent on the pyridine ring in UCB-H with a methyl group leads to the discovery of UCB-J [18], with increased in vitro binding affinity and selectivity for SV2A. In vivo, the radiotracer [^{11}C]UCB-J demonstrated several attractive pharmacokinetic and imaging properties, including fast tissue kinetics, high brain uptake, and high specific binding signals in both nonhuman primates and humans, and has been validated as an imaging biomarker for synaptic density [19–21]. The application of SV2A PET has opened a new avenue for investigating synaptic alterations in a large variety of neurodegenerative and neuropsychiatric disorders [22, 23], and for monitoring the clinical efficacy of disease-modifying therapies [24, 25].

Despite the excellent imaging properties of [^{11}C]UCB-J, the short radioactive half-life (20.4 min) places some restrictions on its broader application, especially in multicenter clinical trials, as its production requires an on-site cyclotron, and distribution to other imaging sites is limited. Thus, we set out to synthesize the longer-lived [^{18}F]-labeled (half-life: 110 min) counterpart of [^{11}C]UCB-J and carried out an in vivo characterization of [^{18}F]UCB-J in nonhuman primates.

Materials and methods

Chemistry

All reagents and solvents were purchased from commercial sources (Sigma-Aldrich, VWR, and Fisher Scientific) and used without further purification. Proton, carbon, and fluorine nuclear magnetic resonance (^{1}H, ^{13}C, and ^{19}F NMR) spectra were recorded on an Agilent 400 MHz or 600 MHz spectrometer (A400a, A400c, or A600a). Chemical shifts are reported in parts per million (ppm), with the solvent resonance as the internal standard ($CDCl_3$: 7.26 ppm; DMSO-d_6: 2.49 ppm in ^{1}H NMR, and $CDCl_3$: 77.0 ppm; DMSO-d_6: 39.7 ppm in ^{13}C NMR). Multiplicities are indicated as s (singlet), d (doublet), t (triplet), q (quartet), quint (quintet), or m (multiplet), with the coupling constant (J) given in hertz (Hz). High-resolution mass spectrometry (HRMS) was performed with a Thermo Scientific LTQ-Orbitrap XL Elite system.

3,5-Difluoro-4-iodobenzonitrile (5) A solution of lithium diisopropylamide (55 mL, 2 M in THF) was added dropwise to a solution of 3,5-difluorobenzonitrile (**4**, 13.7 g, 98.5 mmol) in anhydrous tetrahydrofuran (THF, 130 mL) under argon at −78 °C, followed by a solution of iodine (26.3 g, 103.6 mmol) in anhydrous THF (75 mL). The reaction was slowly warmed to room temperature, stirred for 1 h, and then quenched with 10% sodium thiosulfate solution (100 mL). The mixture was extracted with ethyl acetate (EtOAc)/hexanes (1:1, *v*/v, 50 mL × 3). The combined organic phase was dried over Na_2SO_4 and concentrated in vacuo to afford compound **5** as a brownish solid (10.7 g, 41%), which was used in the next step of synthesis without further purification. ^{1}H NMR ($CDCl_3$, 400 MHz): δ 7.16 (d, J = 5.10 Hz, 2H).

3,5-Difluoro-4-iodobenzaldehyde (6) A solution of diisobutylaluminium anhydride (40.5 mL, 1 M in CH_2Cl_2) was added dropwise to a solution of compound **5** (10.7 g, 40.4 mmol) in anhydrous CH_2Cl_2 (85 mL) under argon at 0 °C. The reaction was slowly warmed to room temperature, stirred for 1 h, and then quenched with 6 N HCl solution (85 mL). The mixture was extracted with CH_2Cl_2 (50 mL × 3). The combined organic phase was dried over Na_2SO_4 and concentrated in vacuo to afford compound **6** as a white solid (9.7 g, 91%), which was used in the next step of synthesis without further purification. ^{1}H NMR ($CDCl_3$, 400 MHz): δ 9.91 (s, 1H), 7.37 (d, J = 5.51 Hz, 2H).

Ethyl-3-(3,5-difluoro-4-iodophenyl)acrylate (7) A solution of carbethoxymethylene triphenylphosphorane (11.0 g, 31.57 mmol) in anhydrous CH_2Cl_2 (50 mL) was added dropwise to a solution of compound **6** (7.70 g, 28.73 mmol) in anhydrous THF (30 mL) under argon at 0 °C. The reaction mixture was stirred for 1 h at 5 °C, and then concentrated in vacuo. A mixture of hexanes and diethyl ether (4:1, *v*/v, 150 mL) was added, and the suspension was stirred for

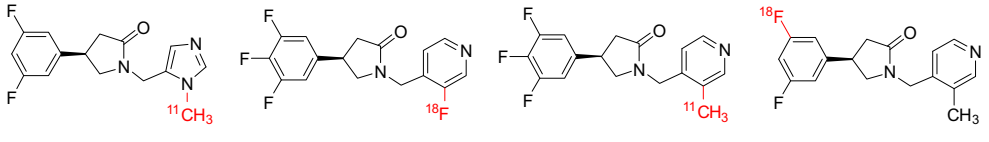

[^{11}C]UCB-A (**1**) [^{18}F]UCB-H (**2**) [^{11}C]UCB-J (**3**) [^{18}F]SDM-8

Fig. 1 PET radiotracers for SV2A

10 min at room temperature. Filtration of the mixture through a silica gel plug and evaporation of the solvents afforded compound **7** as a white solid (9.7 g, quantitative), which was used in the next step of synthesis without further purification. ^{1}H NMR ($CDCl_3$, 400 MHz): δ 7.54 (d, J = 15.94 Hz, 1H), 7.03 (d, J = 6.89 Hz, 2H), 6.45 (d, J = 15.96 Hz, 1H), 4.27 (q, J = 7.09 Hz, 2H), 1.33 (t, J = 7.12 Hz, 3H).

Ethyl 3-(3,5-difluoro-4-iodophenyl)-4-nitrobutanoate (8) Compound **7** (9.76 g, 28.87 mmol) was dissolved in nitromethane (5.0 mL, 93.38 mmol) under argon and cooled at −20 °C. 1,8-Diazabicyclo[5.4.0]undec-7-ene (DBU, 4.8 mL, 32.10 mmol) was added, and the reaction mixture was stirred continuously for 2 h at −20 °C. Water (20 mL) was added, followed by 12 N HCl, until the pH of the mixture reached 1. The mixture was extracted with EtOAc (50 mL × 3). The combined organic phase was dried over Na_2SO_4 and concentrated in vacuo. The crude product was purified on a silica gel column eluting with 0–15% EtOAc/hexanes to afford compound **8** as a white solid (8.3 g, 93%). M.P. 48–50 °C. ^{1}H NMR ($CDCl_3$, 400 MHz): δ 6.80 (d, J = 6.63 Hz, 2H), 4.72 (dd, J = 12.98, 8.40 Hz, 1H), 4.61 (dd, J = 12.98, 6.38 Hz, 1H), 4.12 (q, J = 7.14 Hz, 2H), 3.97 (quint., J = 7.34 Hz, 1H), 2.79–2.65 (m, 2H), 1.21 (t, J = 7.14 Hz, 3H).

4-(3,5-Difluoro-4-iodophenyl)pyrrolidin-2-one (9) NH_4Cl (20.3 g, 386.75 mmol) was added to a suspension of compound **8** (5.0 g, 12.50 mmol) and iron powder (7.0 g, 125.25 mmol) in a mixture of EtOH and water (120 mL, 2:1, *v*/v). After stirring for 16 h at room temperature, the reaction mixture was adjusted to pH 14 with saturated NaOH solution and extracted with EtOAc (50 mL × 3). The combined organic phase was dried over Na_2SO_4 and concentrated in vacuo to afford compound **9** as a white solid (1.88 g, 46%), which was used in the next step of synthesis without further purification. ^{1}H NMR ($CDCl_3$, 400 MHz): δ 6.80 (d, J = 7.60 Hz, 2H), 5.63 (s, 1H), 3.83–3.75 (m, 1H), 3.67 (quint., J = 7.62 Hz, 1H), 3.42–3.30 (m, 1H), 2.74 (dd, J = 17.02, 8.72 Hz, 1H), 2.41 (dd, J = 16.63, 8.10 Hz, 1H).

4-(3,5-Difluoro-4-iodophenyl)-1-((3-methylpyridin-4-yl)methyl)pyrrolidin-2-one (10) Sodium hydride (74 mg, 1.84 mmol) was added to a solution of compound **9** (150 mg, 0.46 mmol) in anhydrous THF (3.0 mL) under argon cooled to 0 °C. Tetrabutylammonium iodide (TBAI, 9 mg, 0.02 mmol) and 4-(chloromethyl)-3-methylpyridine hydrochloride (98 mg, 0.55 mmol) were added after 30 min. The reaction mixture was stirred continuously for 16 h at room temperature, then quenched with saturated $NaHCO_3$ solution (6 mL) and extracted with EtOAc (3 mL × 3). The combined organic phase was dried over Na_2SO_4 and concentrated in vacuo. The crude product was purified on a silica gel column eluting with 0–10% EtOH/EtOAc to afford compound **10** as a light brown solid (128 mg, 65%), M.P. 158–160 °C. ^{1}H NMR ($CDCl_3$, 400 MHz): δ 8.41 (s, 2H), 7.02 (d, J = 4.81 Hz, 1H), 6.72 (d, J = 7.11 Hz, 2H), 4.61 (d, J = 15.42 Hz, 1H), 4.39 (d, J = 15.42 Hz, 1H), 3.70–3.50 (m, 2H), 3.25–3.17 (m, 1H), 2.91 (dd, J = 16.87, 8.61 Hz, 1H), 2.56 (dd, J = 16.86, 7.95 Hz, 1H), 2.30 (s, 3H).

(R,S)-8-((2,6-Difluoro-4-(1-((3-methylpyridin-4-yl)methyl)-5-oxopyrrolidin-3-yl)phenyl)-λ^3-iodanylidene)-6,10-dioxaspiro[4.5]decane-7,9-dione ((R,S)-11) Trifluoroacetic acid (TFA, 0.28 mL, 3.63 mmol), followed by Oxone (75 mg, 0.24 mmol), was added to a solution of compound **10** (52 mg, 0.12 mmol) in $CHCl_3$ (1.0 mL). The reaction mixture was stirred at room temperature for 2 h until it turned to a white suspension. The volatile contents were removed in vacuo. The dried residue was suspended in EtOH (1.0 mL), and 6,10-dioxaspiro[4.5]decane-7,9-dione (SPI-5, 24 mg, 0.14 mmol) was added, followed by 10% Na_2CO_3 solution, until the pH reached 10. The reaction mixture was stirred at room temperature for 2 h, diluted with water (1.0 mL), and extracted with CH_2Cl_2 (1.0 mL × 3). The combined organic phase was dried over Na_2SO_4 and concentrated in vacuo. The crude product was purified on a silica gel column eluting with 10–40% EtOH/EtOAc. Recrystallization of the product in EtOAc/hexanes afforded compound (*R,S*)-**11** as a white solid (22 mg, 31%), M.P. 122–125 °C (decomposition). ^{1}H NMR (DMSO-d_6, 400 MHz): δ 8.37 (s, 2H), 7.27 (d, J = 8.29 Hz, 2H), 7.17 (s, 1H), 4.53 (d, J = 15.69 Hz, 1H), 4.33 (d, J = 15.90 Hz, 1H), 3.78–3.70 (m, 2H), 3.63–3.57 (m, 1H), 2.73 (dd, J = 16.41, 8.90 Hz, 1H), 2.60 (dd, J = 18.45, 11.34 Hz, 1H overlap with DMSO residue peak), 2.20 (s, 3H), 1.89–1.75 (m, 4H), 1.63–1.55 (m, 4H). ^{13}C NMR (DMSO-d_6, 150 MHz): δ 173.2, 173.0 (2C), 163.3 (2C), 162.0, 160.4, 158.3, 158.1, 150.8, 147.9, 144.0, 112.3 (2C), 111.5, 59.7, 53.1, 43.2, 40.5, 37.6, 37.1 (2C), 23.2 (2C), 15.8. ^{19}F NMR (DMSO-d_6, 376 MHz): δ −94.00. HRMS: calculated for $C_{25}H_{23}F_2IN_2O_5$ ($[M+H]^+$), 597.0693; found, 597.0743.

Ethyl 3-(3-bromo-4,5-difluorophenyl)acrylate (13) Compound **13** was prepared according to procedures similar to those described above for compound **7**. Yield: quantitative. ^{1}H NMR ($CDCl_3$, 400 MHz): δ 7.89 (d, J = 15.90 Hz, 1H), 7.42 (m, 2H), 6.29 (d, J = 15.89 Hz, 1H), 4.27 (q, J = 7.12 Hz, 2H), 1.33 (t, J = 7.13 Hz, 3H).

Ethyl 3-(3-bromo-4,5-difluorophenyl)-4-nitrobutanoate (14) Compound **14** was prepared according to procedures similar to those described above for compound **8**. Yield: 80%. ^{1}H NMR ($CDCl_3$, 400 MHz): δ 7.44 (t, J = 8.11 Hz, 1H), 7.10–7.04 (m, 1H), 4.72 (d, J = 6.76 Hz, 2H), 4.37 (quint., J = 6.75 Hz, 1H), 4.10 (q, J = 6.74 Hz, 2H), 2.86–2.74 (m, 2H), 1.20 (t, J = 7.24 Hz, 3H).

4-(3-Bromo-4,5-difluorophenyl)pyrrolidin-2-one (15) Compound **15** was prepared according to procedures similar to those described above for compound **9**. Yield: 64%. ^{1}H NMR ($CDCl_3$, 400 MHz): δ 7.42 (t, J = 8.51 Hz, 1H), 7.19–7.13 (m, 1H), 5.66 (s, 1H), 4.06 (quint., J = 7.25 Hz, 1H), 3.86–3.80 (m, 1H), 3.33–3.28 (m, 1H), 2.78 (dd, J = 17.07, 9.03 Hz, 1H), 2.36 (dd, J = 17.09, 6.68 Hz, 1H).

4-(3-Bromo-4,5-difluorophenyl)-1-((3-methylpyridin-4-yl)methyl)pyrrolidin-2-one (16) Compound **16** was prepared according to procedures similar to those described above for compound **10**. Yield: 33%. M.P. 120–121 °C. ^{1}H NMR ($CDCl_3$, 400 MHz): δ 8.41–8.38 (m, 2H), 7.40 (t, J = 8.48 Hz, 1H), 7.02–6.97 (m, 2H), 4.58–4.46 (m, 2H), 3.94 (quint., J = 7.40 Hz, 1H), 3.70–3.66 (m, 1H), 3.15–3.12 (m, 1H), 2.93 (dd, J = 17.18, 9.13 Hz, 1H), 2.54 (dd, J = 17.16, 6.57 Hz, 1H), 2.29 (s, 3H).

4-(3,4-Difluoro-5-iodophenyl)-1-((3-methylpyridin-4-yl)methyl)pyrrolidin-2-one (17) Copper(I) iodide (27 mg, 0.14 mmol), compound **16** (1.07 g, 2.82 mmol), and sodium iodide (1.69 g, 11.27 mmol) were mixed, and the reaction vessel was evacuated and backfilled with argon three times. A solution of racemic *trans-N,N′*-dimethyl-1,2-cyclohexanediamine (45 μL, 0.29 mmol) in anhydrous 1,4-dioxane (10.0 mL) was added. The reaction mixture was stirred at 120 °C, and conversion was monitored by ^{1}H NMR. One addition of each chemical reagent in 20% of the original amount was added every 24 h. After 72 h of heating, the resulting suspension was cooled to room temperature, diluted with 30% ammonia solution (10 mL), poured into water (30 mL), and extracted with CH_2Cl_2 (15 mL × 3). The combined organic phase was dried over Na_2SO_4 and concentrated in vacuo. The crude product was purified on a silica gel column eluting with 0–15% EtOH/EtOAc to afford compound **17** as a beige solid (0.47 g, 39%), M.P. 115–117 °C. ^{1}H NMR ($CDCl_3$, 400 MHz): δ 8.43–8.40 (m, 2H), 7.64 (t, J = 8.18 Hz, 1H), 7.01 (d, J = 4.89 Hz, 1H), 6.97 (dd, J = 11.40, 7.88 Hz, 1H), 4.58–4.46 (m, 2H), 3.84–3.76 (m, 1H), 3.71–3.65 (m, 1H), 3.13–3.04 (m, 1H), 2.94 (dd, J = 17.26, 9.02 Hz, 1H), 2.49 (dd, J = 17.21, 6.29 Hz, 1H), 2.30 (s, 3H).

(R,S)-(2,3-Difluoro-5-(1-((3-methylpyridin-4-yl)methyl)-5-oxopyrrolidin-3-yl)phenyl)(4-methoxyphenyl)iodonium trifluoromethanesulfonate ((R,S)-18) A solution of compound **17** (150 mg, 0.35 mmol) and anisole (50 μL, 0.46 mmol) in CH_3CN (1 mL) was added to a solution of trifluoromethanesulfonic acid (125 μL, 1.41 mmol) and Oxone (213 mg, 0.69 mmol) in CH_2Cl_2 (1 mL) over 2 h, followed by another portion of Oxone (107 mg, 0.35 mmol). The reaction mixture was stirred at room temperature for 16 h, diluted with H_2O (2 mL), and extracted with CH_2Cl_2 (2 mL × 3). The combined organic phase was dried over Na_2SO_4 and concentrated in vacuo. The residue was purified on a basic alumina column eluting with 0–10% MeOH/CH_2Cl_2 to provide the mono-triflate salt. Recrystallization of the product in CH_2Cl_2/Et_2O afforded compound (*R,S*)-**18** as a light brown solid (50 mg, 27%), M.P. 150–152 °C (decomposition). ^{1}H NMR (DMSO-*d6*, 600 MHz): δ 8.68 (dd, J = 9.52, 7.80 Hz, 1H), 8.8.41–8.34 (m, 2H), 8.16 (d, J = 9.05 Hz, 2H), 7.92 (dd, J = 12.05, 7.90 Hz, 1H), 7.21(d, J = 4.99 Hz, 1H), 7.00(d, J = 9.09 Hz, 2H), 4.55 (d, J = 16.00 Hz, 1H), 4.30 (d, J = 15.97 Hz, 1H), 4.10 (quint, J = 8.55 Hz, 1H), 3.74 (s, 3H), 3.41 (dd, J = 9.71, 8.34 Hz, 1H), 3.18 (dd, J = 9.66, 7.68 Hz, 1H), 2.72 (dd, J = 16.44, 9.00 Hz, 1H), 2.52 (dd, J = 16.43, 8.93 Hz, 1H), 2.24 (s, 3H). ^{13}C NMR (DMSO-d_6, 150 MHz): δ 172.5, 162.5, 150.9, 147.9, 143.9, 143.1, 137.4, 131.9 (2C), 126.6, 126.4, 122.3, 122.2, 118.3, 118.2, 118.0 (2C), 115.9, 106.5, 55.2, 54.0, 43.3, 40.5, 39.2, 15.8; ^{19}F NMR (DMSO-d_6, 564 MHz): δ 77.8 (3F), −129.8 (1F), −135.1 (1F). HRMS: calculated for $C_{25}H_{22}F_5IN_2O_5S$ ($[M + H]^+$), 685.0287; found, 685.0279.

Radiochemistry

$H_2{}^{18}O$ was obtained from Huayi Isotopes (Toronto, Canada). Anion exchange Chromafix cartridges (PS-HCO_3) were purchased from Macherey-Nagel (Düren, Germany). Solid-phase extraction (SPE) C18 Sep-Pak cartridges were purchased from Waters Corporation (Milford, MA, USA).

The high-performance liquid chromatography (HPLC) system used for purification of crude product included a Shimadzu LC-20A pump, a Knauer K-200 UV detector, and a Bioscan gamma-flow detector, with a ChiralCel OD-H semi-preparative column (10 × 250 mm, 5 μm, Chiral Technologies, West Chester, PA, USA) eluting with a mobile phase of 35% CH_3CN and 65% 20 mM ammonium bicarbonate solution (pH 8.6) at a flow rate of 5 mL/min. The HPLC system used for quality control tests comprised a Shimadzu LC-20A pump, a Shimadzu SPD-M20A PDA or SPD-20A UV detector, and a Bioscan gamma-flow detector, with a Genesis C18 column (4.6 × 250 mm, 5 μm) eluting with a mobile phase of 38% CH_3CN and 62% 0.1 M ammonium formate with 0.5% acetic acid (pH 4.2) at a flow rate of 2 mL/min. Identity was confirmed by co-injection of the product with UCB-J (**3**) and detection of a single UV peak on the chromatogram. Enantiomeric purity of the radiolabeled compounds was determined on a ChiralCel OD-H analytical column (4 × 150 mm, 5 μm) eluting with a mobile phase of 35% CH_3CN and 65% 0.1 M ammonium formate with 0.5% acetic acid (pH 4.2) at a flow rate of 1 mL/min.

^{18}F-Fluoride was produced via the ^{18}O(p, n)^{18}F nuclear reaction in a 16.5-MeV PETtrace cyclotron (GE Healthcare, Waukesha, WI, USA). The aqueous ^{18}F-fluoride solution in ^{18}O-water was trapped with a resin cartridge (PS-HCO_3, Macherey-Nagel, Düren, Germany) in a lead-shielded hot cell.

The ^{18}F-fluoride was then eluted with a solution of tetraethylammonium bicarbonate (TEAB, 2 mg) in CH_3CN/H_2O (1 mL, 7:3, *v*/v) into a 5 mL V-Vial (clear borosilicate glass vial sealed with phenolic screw cap; Wheaton Industries/DWK Life Sciences, Millville, NJ, USA) or a NanoTek apparatus (Advion, Louisville, TN). The solvents were azeotropically evaporated at 100 °C, with the addition of two more portions of anhydrous CH_3CN (1 mL). Dried ^{18}F-fluoride was re-dissolved in anhydrous DMF for radiosynthesis. The starting activity was 13.0–22.2 GBq. All the radioactivity and radiochemical yields were reported as measured and not corrected for decay.

(R)- and (S)-4-(3,5-Difluoro-4-(fluoro-^{18}F)phenyl)-1-((3-methylpyridin-4-yl)methyl)pyrrolidin-2-one (4-[^{18}F]UCB-J and (S)-4-[^{18}F]3) A solution of compound (*R,S*)-**11** (2.5 mg) in DMF (0.5 mL) was added to the solution of dried ^{18}F-fluoride-TEAB in DMF (0.5 mL) and the reaction mixture was heated at 170 °C for 10 min. The reaction mixture was diluted with deionized (DI) water (10 mL) and passed through a Waters C18 Sep-Pak cartridge. The cartridge was washed with DI water (10 mL). The crude products were eluted off the cartridge with EtOH (1 mL), diluted with DI water (1 mL), and loaded onto the semi-preparative ChiralCel OD-H column (typical residual activity in the reaction vessel was about 10% of the total after loading of the contents to the HPLC column). The radioactive peak eluting at 19.4 min was the (*S*)-enantiomer (*(S)*-4-[^{18}F]**3**), and the following radioactive peak, eluting at 21.8 min, was the (*R*)-enantiomer (4-[^{18}F]UCB-J). The absolute configuration of UCB-J was previously determined by UCB Pharma [18], and the configuration of the radiotracer [^{18}F]UCB-J and its optically opposite enantiomer was determined by co-injection in HPLC with enantiomeric pure UCB-J reference standard and its other enantiomer provided by UCB.

The HPLC fraction with the desired enantiomer was collected, diluted with DI water (50 mL), and passed through a Waters C18 Sep-Pak cartridge. The cartridge was washed with DI water (10 mL) and dried. The radioactive product, trapped on the cartridge, was recovered by elution with US Pharmacopeial Convention (USP) ethanol (1 mL), followed by USP saline (3 mL). The resulting mixture was then passed through a sterile membrane filter (0.2 μm) for terminal sterilization, and collected in a sterile vial pre-charged with 7 mL of USP saline to afford a formulated solution ready for administration. The radiotracers were stable for at least 1 h after the end of synthesis.

(R)- and (S)-4-(3,4-Difluoro-5-(fluoro-^{18}F)phenyl)-1-((3-methylpyridin-4-yl)methyl)pyrrolidin-2-one (5-[^{18}F]UCB-J and (S)-5-[^{18}F]3) The solution of dried ^{18}F-fluoride-TEAB in DMF (0.5 mL) was loaded into a loop on the NanoTek device and co-infused with compound (*R,S*)-**18** (2.5 mg) in DMF (0.5 mL) through a microreactor (2 m coiled glass silica tube with 100 μm internal diameter; 15.7 μL) at a set flow rate and temperature. Optimization was performed by changing the precursor concentration, reactor temperature, and flow rates to obtain the best incorporation of ^{18}F-fluoride. Incorporation yield was calculated based on radio-HPLC analysis using a Luna C18 column (4.6 × 250 mm, 5 μm; Phenomenex, Torrance, CA). The best reaction parameters for the NanoTek reactor were found to be a flow rate of 50 μL/min for both the solutions of compound (*R,S*)-**18** and ^{18}F-fluoride at a reaction temperature of 200 °C. Purification and formulation procedures were the same as those described above for 4-[^{18}F]UCB-J.

PET imaging experiments in rhesus monkeys

PET scan procedures PET imaging experiments were performed in rhesus monkeys (*Macaca mulatta*) according to a protocol approved by the Yale University Institutional Animal Care and Use Committee. Three monkeys (2 male, 1 female) were used in a total of five 120-min scans, including two baseline scans with 5-[^{18}F]UCB-J (female monkey and male monkey A), one baseline scan with 4-[^{18}F]UCB-J (male monkey B), one baseline scan with the inactive enantiomer *(S)*-5-[^{18}F]**3** (female monkey), and one self-blocking scan with 5-[^{18}F]UCB-J using UCB-J (**3**, 0.15 mg/kg, male monkey A) administered as a 10-min infusion starting 10 min before radiotracer injection to verify the binding specificity. One additional 180-min scan with 5-[^{18}F]UCB-J (male monkey A) was carried out to evaluate the displacement effect, in which SV2A specific ligand levetiracetam (30 mg/kg) was given as a 5-min infusion at 90 min post-radiotracer injection. In addition, four baseline scans with [^{11}C]UCB-J were conducted in these three monkeys for comparison purpose.

In preparation for each scan, the monkey was subjected to fasting overnight, and immobilized with ketamine (10 mg/kg, intramuscularly) at least 2 h prior to the PET scan. A venous line was inserted for administration of radiotracer and blocking/displacement drug in one limb. A catheter was placed in the femoral artery in the other limb for blood sampling. Endotracheal intubation was performed to enable administration of isoflurane (1.5–2.5% in oxygen). A water-jacket heating pad was used to maintain body temperature. The animal was attached to a physiological monitor, and vital signs (heart rate, blood pressure, respiration, SPO2, EKG, ETCO2, and body temperature) were monitored continuously.

Dynamic PET scans were performed on a Focus 220 scanner (Siemens Medical Solutions, Knoxville, TN, USA) with a reconstructed image resolution of approximately 1.5 mm. Before radiotracer injection, a 9-min transmission scan was obtained for attenuation correction. The radiotracer was administered by an infusion pump over 3 min. Emission data were collected in list mode for 120 min and reformatted into

33 successive frames of increasing duration (6 × 30 s, 3 × 1 min, 2 × 2 min, and 22 × 5 min). For the 180-min scan, additional frames (12 × 5 min) were acquired.

Plasma metabolite analysis and input function measurement Arterial blood samples were collected at preselected time points and assayed for radioactivity in whole blood and plasma with cross-calibrated well-type gamma counters (Wizard 1480/2480, Perkin Elmer, Waltham, MA, USA). Seven samples, drawn at 0, 5, 15, 30, 60, 90 and 120 min, were processed and analyzed to measure radioactive metabolites by HPLC analysis using the column-switching method [26]. Whole blood samples in EDTA tubes were centrifuged at 2930×*g* at 4 °C for 5 min to separate the plasma. Supernatant plasma was collected, and activity in 0.2 mL aliquots was counted on a gamma counter. Plasma samples were then mixed with urea (8 M) to denature the plasma proteins, filtered through a 1.0 μm Whatman 13 mm CD/X syringe filter, and loaded onto an automatic column-switching HPLC system connecting a capture column (4.6 × 19 mm) self-packed with Phenomenex Strata-X polymeric SPE sorbent and eluting with 1% CH_3CN/water at 2 mL/min for 4 min. The trapped activity in the capture column was then back-flushed and eluted through a Gemini-NX column (4.6 × 250 mm, 5 μm) with 40% CH_3CN in 0.1 M ammonium formate (pH = 6.4) solution at a flow rate of 1.55 mL/min. The eluent fractions were collected with an automated fraction collector (Spectrum Chromatography CF-1). Radioactivity in the whole blood, plasma, filtered plasma–urea mix, filter, and HPLC eluent fractions was all counted with the automatic gamma counters. The sample recovery rate, extraction efficiency, and HPLC fraction recovery were monitored. The un-metabolized parent fraction was determined as the ratio of the sum of radioactivity in fractions containing the parent compound to the total amount of radioactivity collected, and fitted with inverted gamma function and corrected for filtration efficiency. The arterial plasma input function was then calculated as the product of the total counts in the plasma and the interpolated parent fraction at each time point, and was used in the analysis of brain time–activity curves and the calculation of binding parameters with kinetic models.

Measurement of radiotracer free fraction (f_p) in plasma An ultrafiltration method was used for measuring the unbound portion (free fraction) of [^{18}F]UCB-J in plasma, as previously described [27]. The f_P was determined as the ratio of the radioactivity concentration in the filtrate to the total activity in plasma. Measurements of f_P were performed in triplicate for each scan.

Imaging analysis and kinetic modeling High-resolution magnetic resonance (MR) images were acquired with a Siemens 3T Trio scanner to assist with image co-registration and anatomical localization of regions of interest (ROIs). The MR image was registered to an atlas and to the PET images, as previously described [28].

PET data were corrected for attenuation, scanner normalization, scatter, and random events, and dynamic images were reconstructed using a Fourier rebinning and filtered back-projection algorithm. Using the MR images, the following ROIs were defined: amygdala, brainstem, caudate nucleus, centrum semiovale, cerebellum, cingulate cortex, frontal cortex, globus pallidus, hippocampus, insula, nucleus accumbens, occipital cortex, pons, putamen, temporal cortex, and thalamus. For each PET scan, radiotracer concentrations over time, i.e., time–activity curves (TACs), were generated for the ROIs.

Regional TACs were fitted and analyzed with the one-tissue compartment (1TC) model [29], which has been shown to be a reliable model with low standard error (SE), as described previously [19]. Regional distribution volume (V_T, mL/cm^{-3}) was calculated from kinetic analysis of regional TACs using the metabolite-corrected arterial plasma concentration as the input function [30].

Non-displaceable binding potential (BP_{ND}) was calculated from regional V_T values using centrum semiovale as the reference region, i.e., $BP_{ND} = (V_{T,\,ROI} - V_{T,\,semiovale})/V_{T,\,semiovale}$.

SV2A occupancy by UCB-J was obtained from the occupancy plot using the regional V_T from the baseline scan and V_T difference between baseline and blocking scans [31].

Results

Chemistry

The presence of three fluorine atoms on the benzene ring of UCB-J (**3**) allows the placement of an ^{18}F-label on the molecule without changing the chemical structure. Our initial efforts to effect radiofluorination through traditional nucleophilic substitution of iodo or chloro leaving groups, however, were not successful. Instead, they resulted in isotopically exchanged products exclusively, likely due to the mutual activation of the fluorine atoms (Scheme 1). Not surprisingly, treatment of UCB-J with ^{18}F-fluoride under the same radiolabeling conditions also led to an isotopically exchanged product, presumably with ^{18}F on the 4-position of the benzene ring, in its racemic form and with low molar activity.

We then turned to a new radiofluorination method using hypervalent iodonium precursors for the radiosynthesis of [^{18}F]UCB-J [32–34]. Two precursors (compounds **11** and **18**) were prepared for radiofluorination. Iodonium ylide precursor **11** was prepared from a seven-step synthesis, with ~3.2% overall yield (Scheme 2). 3,5-Difluorobenzonitrile (**4**) was iodinated and reduced to form 3,5-difluoro-4-iodobenzaldehyde (**6**), which underwent a Wittig reaction to

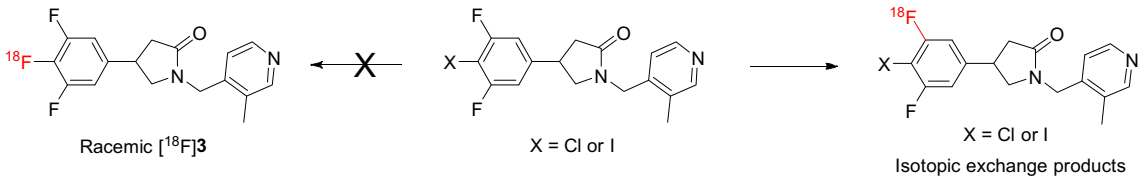

Scheme 1 Attempted radiosynthesis of [^{18}F]UCB-J ([^{18}F]-**3**) from chloro or iodo precursor.

form the α,β-unsaturated ester (**7**). Michael addition with nitromethane then provided compound **8**, followed by reduction with iron powder under mildly acidic conditions. The reduction with iron powder can be completed either at elevated temperature in 3 h or at room temperature for an extended reaction time. The iodine at the 4-position in compound **8**, however, did not survive the reaction at elevated temperature. Therefore, this reduction was carried out at room temperature for 16 h, followed by in situ cyclization with the addition of saturated NaOH solution to afford compound **9**. Interestingly, this cyclization can only be achieved with saturated NaOH, and the use of less concentrated NaOH solution or other bases to quench the reaction resulted in only trace amounts of the product **9**. Coupling with 4-(chloromethyl)-3-methylpyridine then gave compound **10**. Finally, the iodonium ylide **11** was prepared from compound **10** following previously reported procedures [33]. Trituration with EtOAc and hexanes afforded the iodonium ylide precursor **11** as a white powder.

Synthesis of the iodonium salt precursor **18** (Scheme 3) started with 3-bromo-4,5-difluorobenzaldehyde (**12**) and followed similar steps as those described above to prepare compound **16**. Compound **16** was converted to the iodo compound **17** using the copper-catalyzed aromatic Finkelstein reaction [35]. Formation of the iodonium salt **18** was achieved using procedures modified from Bielawski et al. [36], which indicated that the purification of iodonium salt on Al_2O_3 would lead to a mono-triflate iodonium salt. The prepared iodonium salt was further tested with ^{19}F-NMR analysis and determined as the mono-triflate using the integration of fluorine peaks on the ^{19}F-NMR spectrum.

We also prepared a few other precursors (**19**–**21**) to test the radiofluorination methodologies and conditions that have been reported recently, for example PhenoFluor-mediated deoxyfluorination through concerted nucleophilic substitution [37] and copper-catalyzed fluorination with arylstannanes through single electron transfer [38], and to compare with the hypervalent iodonium precursors.

Radiochemistry

With conventional heating, three radiofluorination temperatures (120, 150 and 170 °C) were tested with the 4-iodonium ylide precursor **11**, and the radiochemical yield gradually increased with increasing temperature (Scheme 4). The same results were obtained with the 5-iodonium salt precursor **18**.

We further optimized the radiofluorination conditions with precursor **18** using the NanoTek microfluidic reactor. A screening of radiolabeling conditions indicated DMF as the preferred reaction solvent for the radiosynthesis of 5-[^{18}F]UCB-J from the iodonium salt precursor **18**. Similar to reaction with conventional heating, the rate of ^{18}F incorporation gradually increased when the reaction temperature was increased from 120 °C to 200 °C with different flow rates and precursor-to-fluoride ratios in the microfluidic reactor. The best conditions for ^{18}F incorporation were found to be reaction at 200 °C, with flow rate of 50 μL/min for both the precursor and ^{18}F-fluoride solutions (78% incorporation based on radio-HPLC). The HPLC yield was calculated from the radiochromatogram. It is worth noting, though, that this yield was apparently overestimated when compared with the isolated yield, as there was most likely significant retention of radioactivity on the HPLC column, and recovery of activity was not checked during these test runs.

Radiofluorination simulation with UCB-J was conducted under these established optimal microfluidic flow rates to check for racemization, and showed complete racemization of the compound at temperatures higher than 120 °C in the presence of the base TEAB (1 mg/mg of UCB-J). As a result,

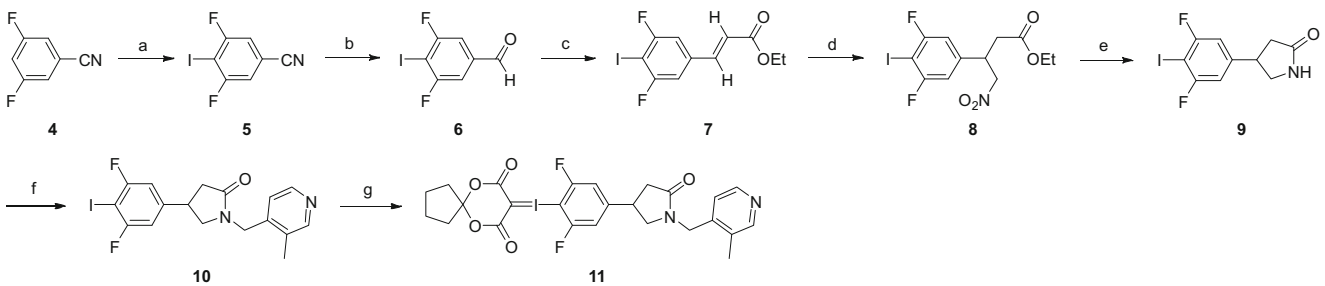

Scheme 2 Synthesis of racemic 4-iodonium ylide precursor (**11**).

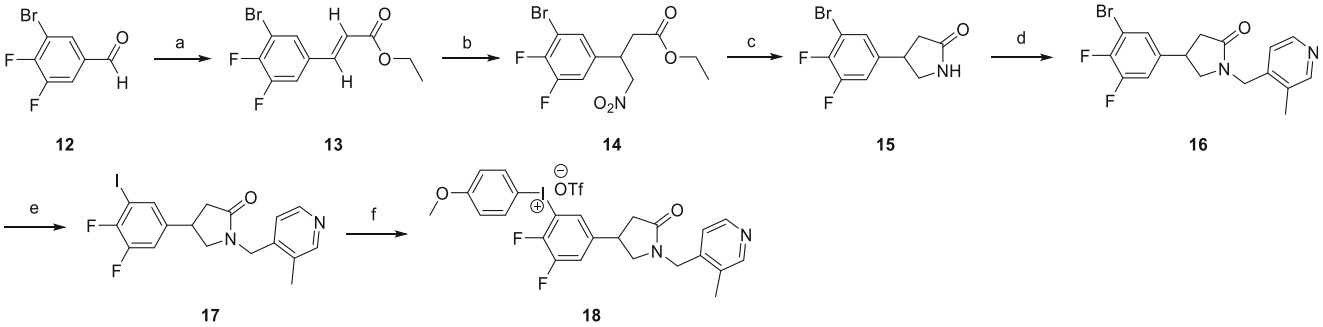

Scheme 3 Synthesis of racemic 5-iodonium salt precursor (**18**).

^{18}F-fluorination was performed with racemic iodonium precursors on the Nanotek microfluidic reactor, or manually in a hot cell at elevated temperatures (200 °C for the microfluidic reactor; and 170 °C for manual synthesis), followed by purification on a semi-preparative chiral HPLC column to resolve the two enantiomers. Total synthesis time was ~120 min including purification and formulation. The radiotracers were prepared in >99% radiochemical purity and enantiomeric purity (Fig. 2). Isolated radiochemical yield (RCY) for the desired enantiomer was low, at 1–2%, and molar activity at the end of synthesis was moderate (59.0 ± 35.7 MBq/nmol, $n = 5$).

Employing the procedures reported in the literature (Scheme 5), the racemic hydroxy-complex precursor (**19**) produced the racemic product *(R,S)*-[^{18}F]**3** in ~ 5% RCY (HPLC incorporation yield, decay-uncorrected), similar to the results from hypervalent iodonium precursors, while the trimethyltin precursors (**20** and **21**) did not produce *(R,S)*-[^{18}F]**3** in detectable RCY.

PET imaging experiments in rhesus monkeys

Injection parameters A total of six PET scans were performed in three different monkeys. Mean injected radioactivity was 57.3 MBq, with mean injected mass of 0.31 μg.

Plasma analysis The results from plasma analysis are shown in Fig. 3. [^{18}F]UCB-J displayed a moderate rate of change over time in plasma, with 51 ± 8% of intact parent radiotracer at 30 min after injection, which decreased to 35 ± 2% and 27 ± 2% at 60 and 90 min, respectively ($n = 4$). After a bolus injection, the parent radioactivity level in plasma exhibited a quick increase to peak and a sharp decline phase within 5 min, then a slow decrease afterwards. On the reversed-phase HPLC chromatograms (Fig. 3c), the observed metabolite peaks were more polar than the parent (retention time of ~ 7 min for metabolites vs. ~ 11 min for the parent radiotracer). The f_p of the radiotracer in plasma was 42 ± 6% ($n = 4$), similar to that measured with [^{11}C]UCB-J (43 ± 5%, $n = 4$).

Brain analysis Representative PET images summed from 20 to 40 min post-injection are shown in Fig. 4. In the baseline scan (Fig. 4c), high uptake was seen throughout the gray matter regions, and lower uptake in the centrum semiovale (white matter) region, similar to that of [^{11}C]UCB-J (Fig. 4b). A clear reduction in radiotracer uptake was observed in the self-blocking scan (Fig. 4d).

Brain kinetics of [^{18}F]UCB-J were fast and reversible. Regional TACs for [^{18}F]UCB-J indicated excellent radiotracer uptake in the monkey brain, with a peak standard uptake value (SUV) of ~12 at 20–30 min post-injection (Fig. 5a). The highest radioactivity concentrations were observed in the

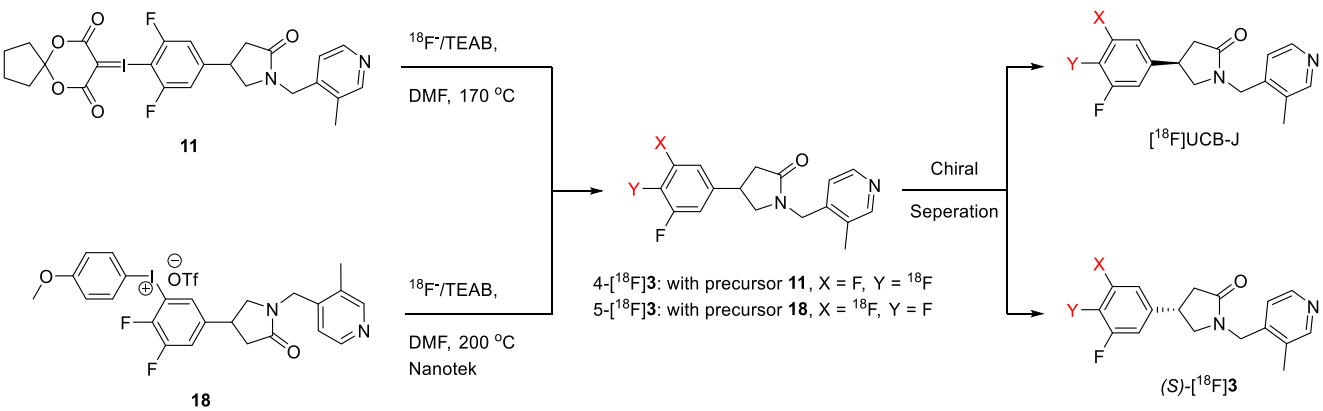

Scheme 4 Radiosynthesis and chiral separation of [^{18}F]UCB-J and *(S)*-[^{18}F]**3**.

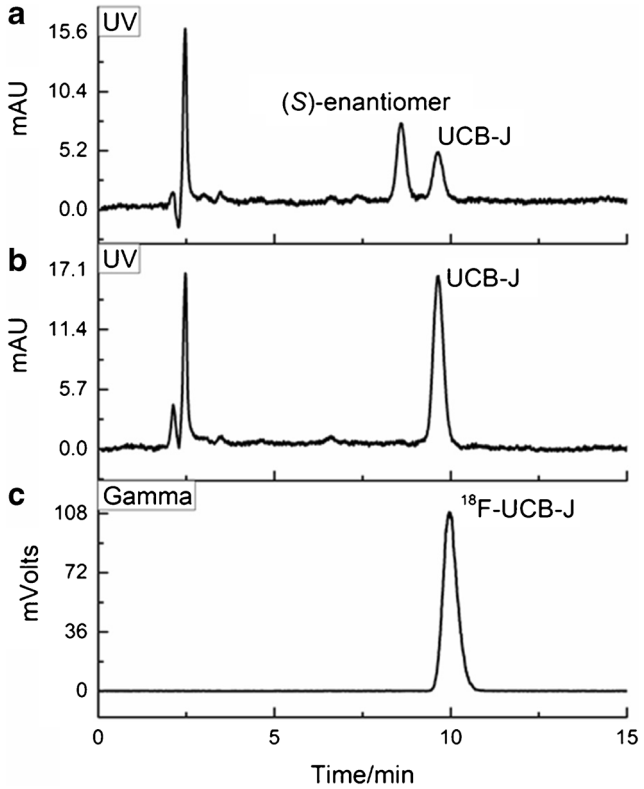

Fig. 2 HPLC chromatograms for (*R,S*)-**3** (A), UCB-J (B) and [^{18}F]UCB-J (C)

frontal cortex and putamen, while the lowest uptake was seen in the centrum semiovale. Self-blocking with UCB-J at a dose of 0.15 mg/kg resulted in earlier peak uptake within 10 min and a rapid decrease thereafter, with greatly reduced differences in regional activity levels (Fig. 5b). Displacement with the SV2A specific ligand levetiracetam at 90 min after radiotracer administration resulted in a rapid reduction in radiotracer binding, leading to fairly homogeneous uptake across the brain regions (Fig. 5c). As expected, a baseline scan with the other enantiomer, *(S)*-5-[^{18}F]**3**, displayed homogeneous regional uptake similar to that of the self-blocking scan with 5-[^{18}F]UCB-J (compare Fig. 5d to b).

Regional TACs were analyzed with the 1TC model using the metabolite-corrected plasma radioactivity as input function to calculate binding parameters. The 1TC model produced good fits of the TACs and reliable estimates of regional V_T. Values of V_T were highest in cortical regions, followed by caudate, putamen, and thalamus, and lowest in white matter (Table 1). An apparent reduction in regional V_T values was seen in the self-blocking scan, while the inactive enantiomer exhibited V_T values largely indistinguishable among the brain regions, reflecting non-specific binding. The rank order and magnitude of the calculated BP_{ND} values (Table 2) in various brain regions were similar between [^{18}F]UCB-J and [^{11}C]UCB-J in the same monkeys.

In the self-blocking study, pretreatment with 0.15 mg/kg of UCB-J at 10 min before 5-[^{18}F]UCB-J injection greatly reduced regional V_T and BP_{ND} values across the monkey brain regions (Tables 1 and 2). Occupancy by UCB-J was calculated at 73%, similar to that produced by the same dose of UCB-J with [^{11}C]UCB-J (87%) [19].

Discussion

We previously reported [^{11}C]UCB-J as a PET radiotracer for SV2A with high specific binding signals in nonhuman primates and humans [19, 20], and have demonstrated its use as a valid biomarker for quantification of synaptic density [20]. In this study, we describe the synthesis and in vivo evaluation of [^{18}F]UCB-J in rhesus monkeys, and its comparison with [^{11}C]UCB-J.

The radiosynthesis of [^{18}F]UCB-J appeared to be challenging, and initial attempts using the chloro/iodo precursors failed to produce [^{18}F]UCB-J. Instead, a product resulting from isotopic exchange was formed.

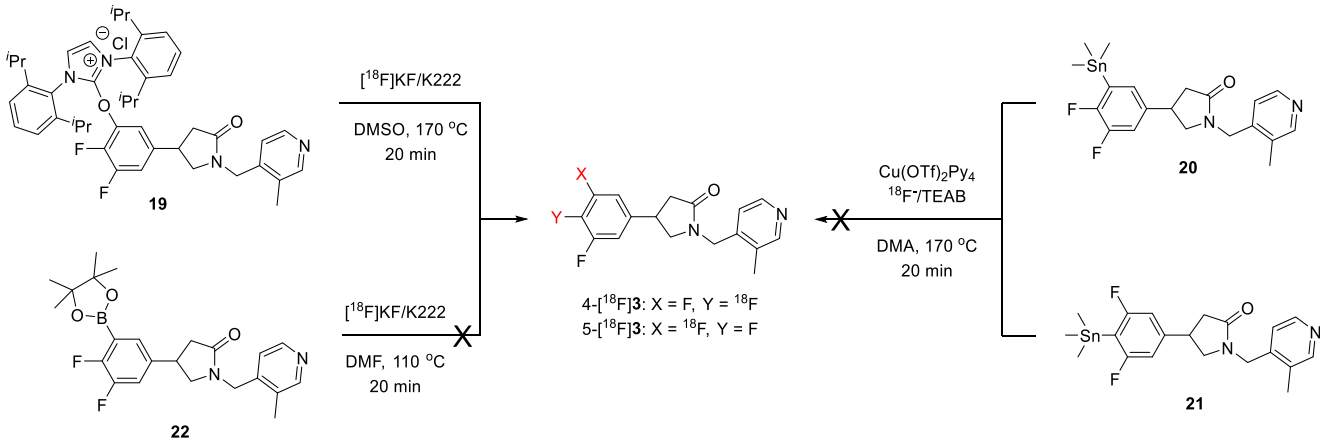

Scheme 5 Radiosynthesis of racemic [^{18}F]**3** with boronic ester, phenol-complex, and arylstannanes precursors.

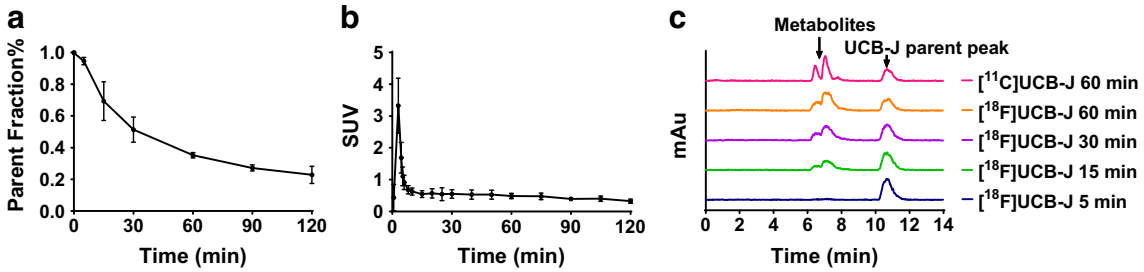

Fig. 3 Parent fraction of [^{18}F]UCB-J in plasma (**a**), metabolite-corrected plasma radioactivity (**b**) over time ($n = 4$, mean ± SD), and metabolite analysis of 5-[^{18}F]UCB-J at selected time points in comparison with [^{11}C]UCB-J (C)

Recent developments in radiofluorination methodologies using boron, iodonium, sulfonium, or tin precursors [37–40] provide new ways to synthesize radiotracers that cannot be readily accessed through conventional radiofluorination approaches. Thus, we carried out a preliminary investigation of radiofluorination (Scheme 5) with the boronic ester *t*-butyl 4-[3,4-difluoro-5-(4,4,5,5-tetramethyl-1,3,2-dioxaborolan-2-yl)phenyl]-2-oxo-pyrrolidine-1-carboxylate (**22**) using the copper-mediated ^{18}F-labeling conditions described by Tredwell et al. [41]. However, no ^{18}F-labeled product was observed, indicating that [^{18}F]UCB-J may not be accessible through boron precursors.

We next turned to the use of hypervalent iodonium precursors. A few iodonium precursors were thus synthesized, with good overall yield and purity. In the end, [^{18}F]UCB-J, labeled at either the 4- or 5-position, was successfully produced using iodonium precursors under conventional heating or microfluidic reaction conditions. Nonetheless, the isolated radiochemical yield was still low, at 1–2%. In this initial study, we did not perform further optimization to improve the label-

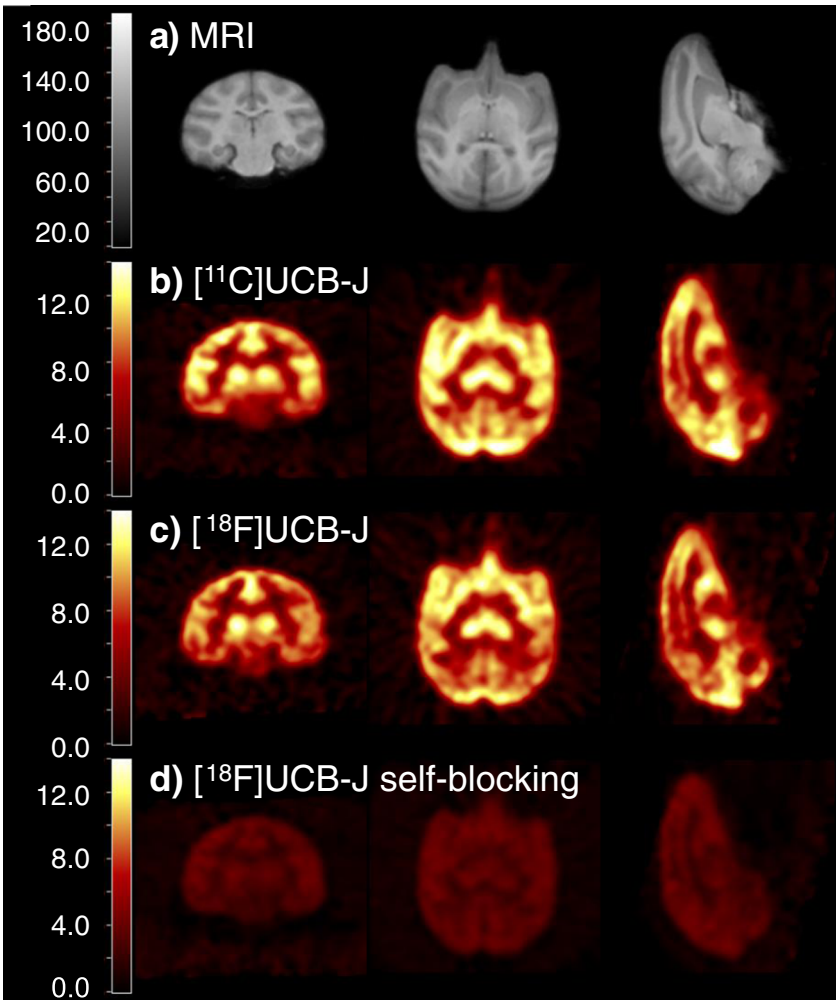

Fig. 4 Template MRI (**a**) and representative summed PET images (20–40 min post-injection) from a [^{11}C]UCB-J baseline scan (**b**), a [^{18}F]UCB-J baseline scan (**c**), and a self-blocking scan (with 0.15 mg/kg UCB-J, **d**)

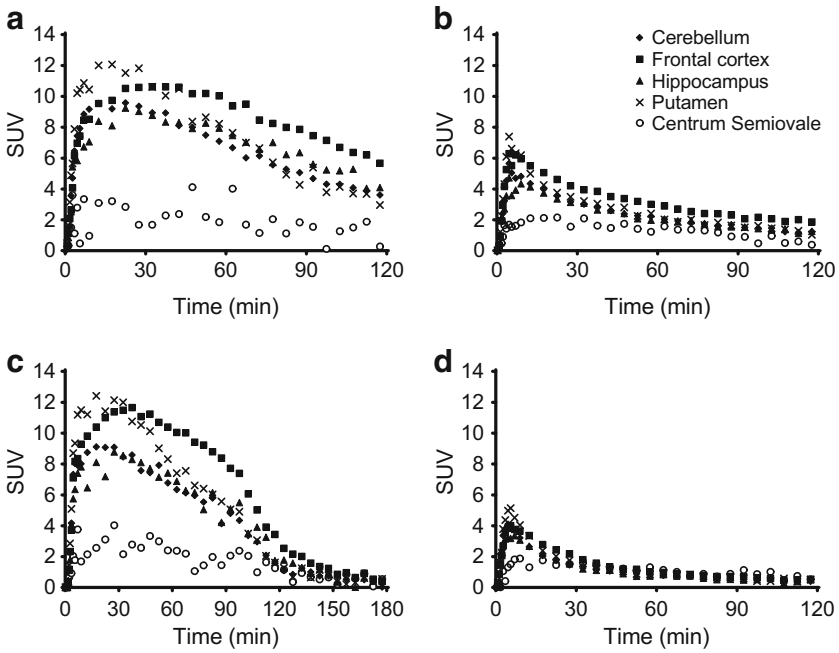

Fig. 5 Regional time–activity curves: (**a**) [^{18}F]UCB-J baseline scan; (**b**) [^{18}F]UCB-J self-blocking scan (with 0.15 mg/kg of UCB-J); (**c**) [^{18}F]UCB-J baseline scan followed by displacement with levetiracetam (30 mg/kg, given i.v. at 90 min); (**d**) baseline scan with *(S)*-5-[^{18}F]**3**

ing yield, as the current yield of [^{18}F]UCB-J was sufficient for PET imaging studies in nonhuman primates to assess its in vivo binding and pharmacokinetic properties for comparison with [^{11}C]UCB-J.

Further radiolabeling studies with the phenol-complex precursor as well as the arylstannane precursors did not improve the radiochemical yield of [^{18}F]UCB-J.

In rhesus monkeys, [^{18}F]UCB-J displayed a moderate rate of change in plasma, similar to that of [^{11}C]UCB-J. Plasma f_p of [^{18}F]UCB-J was high and can be reliably measured. The radiotracer readily entered the monkey brain and accumulated with high concentrations throughout the gray matter regions. Regional TACs demonstrated fast and reversible kinetics, with peak uptake reached within 30 min post-injection in all brain

Table 1 Regional distribution volume (V_T) from baseline scans of [^{18}F]UCB-J ($n = 4$)* and (*S*)-5-[^{18}F]**3** ($n = 1$), as well as a self-blocking scan of [^{18}F]UCB-J with 0.15 mg/kg UCB-J ($n = 1$), in comparison with those from [^{11}C]UCB-J baseline scans ($n = 4$)

Brain region	V_T (mL/cm^{-3})			
	[^{18}F]UCB-J baseline	[^{18}F]UCB-J self-blocking	*(S)*-5-[^{18}F]**3** baseline	[^{11}C]-UCB-J baseline
Amygdala	24.1 ± 6.4	10.6	5.0	24.1 ± 2.2
Brainstem	17.3 ± 2.1	8.7	5.7	20.1 ± 2.8
Caudate	33.1 ± 3.4	13.5	6.6	40.3 ± 6.1
Cerebellum	26.9 ± 1.7	11.6	5.7	30.5 ± 3.5
Cingulate cortex	47.9 ± 7.9	16.0	7.2	47.3 ± 7.5
Frontal cortex	46.2 ± 6.1	16.2	7.2	48.9 ± 7.4
Globus pallidus	19.2 ± 4.3	10.6	6.3	24.5 ± 3.1
Hippocampus	27.6 ± 3.8	11.3	5.7	31.3 ± 2.3
Insula	42.5 ± 5.5	14.8	6.8	47.7 ± 7.5
Nucleus accumbens	45.7 ± 5.9	15.8	6.3	45.7 ± 6.2
Occipital cortex	41.3 ± 6.6	13.4	6.6	45.1 ± 6.9
Pons	17.0 ± 2.6	8.5	6.1	19.8 ± 2.7
Putamen	34.3 ± 5.3	12.3	6.6	40.1 ± 6.8
Centrum semiovale	9.5 ± 1.7	6.9	6.9	11.1 ± 1.6
Temporal cortex	39.2 ± 5.6	12.8	6.5	42.8 ± 6.7
Thalamus	32.3 ± 7.3	14.0	6.3	36.2 ± 5.2

*Data are from three baseline scans with 5-[^{18} F]UCB-J including the first 90 min of data in the displacement scan, and one baseline scan with 4-[^{18} F]UCB-J

Table 2 Regional non-displaceable binding potential (BP_{ND}) values from [^{18}F]UCB-J baseline scans ($n = 4$)* and a self-blocking scan of [^{18}F]UCB-J with 0.15 mg/kg UCB-J ($n = 1$), in comparison with those from [^{11}C]UCB-J baseline scans ($n = 4$)

Brain region	BP_{ND}		
	[^{18}F]UCB-J baseline	[^{11}C]UCB-J baseline	[^{18}F]UCB-J self-blocking
Amygdala	1.7 ± 0.9	1.2 ± 0.4	0.5
Brainstem	0.8 ± 0.2	0.8 ± 0.2	0.3
Caudate	2.5 ± 0.5	2.7 ± 0.7	1.0
Cerebellum	1.9 ± 0.4	1.8 ± 0.3	0.7
Cingulate cortex	4.0 ± 0.3	3.3 ± 0.9	1.3
Frontal cortex	3.9 ± 0.5	3.5 ± 0.9	1.3
Globus pallidus	1.1 ± 0.5	1.2 ± 0.2	0.5
Hippocampus	2.0 ± 0.7	1.9 ± 0.3	0.6
Insula	3.5 ± 0.5	3.3 ± 0.8	1.1
Nucleus accumbens	3.9 ± 0.5	3.2 ± 0.7	1.3
Occipital cortex	3.4 ± 0.2	3.1 ± 0.7	0.9
Pons	0.8 ± 0.2	0.8 ± 0.2	0.2
Putamen	2.6 ± 0.4	2.6 ± 0.5	0.8
Temporal cortex	3.1 ± 0.4	2.9 ± 0.6	0.9
Thalamus	2.5 ± 1.0	2.3 ± 0.7	1.0

*Data are from three baseline scans with 5-[^{18} F]UCB-J including the first 90 min of data in the displacement scan, and one baseline scan with 4-[^{18} F]UCB-J

regions. A baseline scan of the inactive enantiomer *(S)*-5-[^{18}F]**3** indicated a lack of specific binding for the compound and thus the chiral selectivity of radiotracer binding to SV2A, consistent with its low binding affinity to human SV2A protein (pIC_{50} of 7.1 for the (*S*)-enantiomer versus 8.2 for the (*R*)-enantiomer UCB-J) [18]. In the self-blocking study, pretreatment of the animal with UCB-J (0.15 mg/kg) greatly reduced the binding of [^{18}F]UCB-J across all brain regions, thus demonstrating the radiotracer's binding specificity in vivo. In the displacement study, administration of the SV2A-selective anticonvulsant levetiracetam at 90 min post-injection resulted in a rapid reduction in [^{18}F]UCB-J binding across gray matter regions, indicating competition of the displacing drug for the same binding target. These results confirmed the saturable, reversible, and specific nature of [^{18}F]UCB-J binding for SV2A in vivo.

Previous studies with [^{11}C]UCB-J indicated that the 1TC model was an appropriate model for the estimation of binding parameters. This was also true for [^{18}F]UCB-J, with the 1TC model producing good fits of regional TACs and stable V_T estimates. As expected, binding of [^{18}F]UCB-J was seen in gray matter areas, with high V_T values in cortical areas and the lowest V_T in the centrum semiovale (white matter), consistent with autoradiography and in vitro binding results [42].

Given the equivalent chemical structure of [^{18}F]UCB-J and [^{11}C]UCB-J, the two radiotracers behaved very similarly when evaluated in the same monkeys, in terms of metabolism and clearance (parent fraction of 51 ± 8% for [^{18}F]UCB-J vs. 47 ± 12% for [^{11}C]UCB-J at 30 min post-injection), plasma free fraction (42 ± 6% vs. 43 ± 5%), brain uptake kinetics, regional distribution, and specific binding signals as measured by BP_{ND} (Fig. 6 and Table 2). Both [^{18}F]UCB-J and [^{11}C]UCB-J provide BP_{ND} values of >0.75 in all brain regions, levels of specific binding signals that can be reliably and accurately estimated by quantitative kinetic modeling analysis, and one of the important characteristics for an effective neuroimaging radiotracer [43].

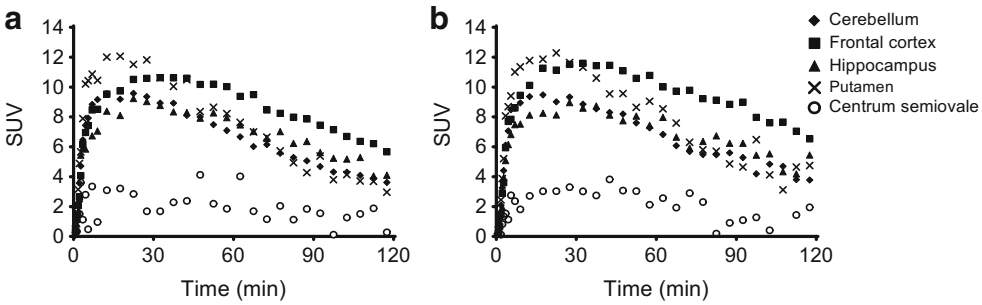

Fig. 6 Regional time–activity curves of [^{18}F]UCB-J (**a**) and [^{11}C]UCB-J (**b**) in the same rhesus monkey brain ($n = 1$)

Although [^{18}F]UCB-J was proved to be an excellent radiotracer, its radiosynthesis is low-yielding. Thus, we conclude that clinical translation of [^{18}F]UCB-J would be challenging unless alternative approaches to its radiosynthesis in high radiochemical yield could ultimately be found. As a result, we have turned to look for alternative [^{18}F]-labeled SV2A radiotracers. Removal of one or two fluorine atoms on the phenyl moiety of the UCB-J structure led to the discovery of SDM-8 and SDM-2, both of which displayed good in vitro binding affinity for SV2A [44]. We recently reported the successful synthesis of [^{18}F]SDM-8 (Fig. 1) with greatly improved radiochemical yield using the organotin precursor [45]. Imaging evaluation in nonhuman primates indicated that [^{18}F]SDM-8 exhibited pharmacokinetic and binding profiles similar to those of [^{18}F]UCB-J, and with higher specific binding signals (BP_{ND}). The same radiolabeled compound, but with a different name (MNI-1126), was reported by another group [46]. Based on the results in nonhuman primates, we anticipate that [^{18}F]SDM-8 will be an excellent [^{18}F]-labeled radiotracer for imaging of SV2A, and have advanced it to evaluation in humans.

Conclusions

We have successfully developed a novel ^{18}F-labeled PET radiotracer for SV2A imaging, and have carried out a detailed evaluation in rhesus monkeys. [^{18}F]UCB-J demonstrated the desirable pharmacokinetic and in vivo binding characteristics of an effective PET imaging agent. A side-by-side comparison of [^{18}F]UCB-J and [^{11}C]UCB-J indicates similar kinetic and binding profiles for these two radiotracers. Although the radiofluorination still needs additional optimization, with a longer half-life, [^{18}F]UCB-J offers the potential feasibility of central production and distribution to off-site locations for use in multicenter clinical trials. Since SV2A has been demonstrated to be an in vivo biomarker for synaptic density, PET imaging with an ^{18}F-labeled SV2A radiotracer is expected to find great utility in clinical studies investigating neurodegenerative disorders and psychiatric diseases, as well as in the monitoring of treatment efficacy for therapies targeted at the repair and recovery of synaptic density.

Acknowledgements The authors thank the staff at the Yale PET Center for their expert assistance in this work. Z.C. was supported by the NIH/NIBIB under award number K01 EB023312.

Compliance with ethical standards

Conflict of interest The authors declare that they have no conflict of interest.

Ethical approval All procedures performed in studies involving animals were in accordance with the ethical standards of the Yale University Institutional Animal Care and Use Committee.

References

1. Loscher W, Gillard M, Sands ZA, Kaminski RM, Klitgaard H. Synaptic vesicle glycoprotein 2A ligands in the treatment of epilepsy and beyond. CNS Drugs. 2016;30:1055–77. https://doi.org/10.1007/s40263-016-0384-x.
2. Bajjalieh SM, Peterson K, Shinghal R, Scheller RH. SV2, a brain synaptic vesicle protein homologous to bacterial transporters. Science. 1992;257:1271–3. https://doi.org/10.1126/science.1519064.
3. Crowder KM, Gunther JM, Jones TA, Hale BD, Zhang HZ, Peterson MR, et al. Abnormal neurotransmission in mice lacking synaptic vesicle protein 2A (SV2A). Proc Natl Acad Sci U S A. 1999;96:15268–73. https://doi.org/10.1073/pnas.96.26.15268.
4. Mendoza-Torreblanca JG, Vanoye-Carlo A, Phillips-Farfan BV, Carmona-Aparicio L, Gomez-Lira G. Synaptic vesicle protein 2A: basic facts and role in synaptic function. Eur J Neurosci. 2013;38:3529–39. https://doi.org/10.1111/ejn.12360.
5. Feng G, Xiao F, Lu Y, Huang Z, Yuan J, Xiao Z, et al. Downregulation synaptic vesicle protein 2A in the anterior temporal neocortex of patients with intractable epilepsy. J Mol Neurosci. 2009;39:354–9. https://doi.org/10.1007/s12031-009-9288-2.
6. Tokudome K, Okumura T, Shimizu S, Mashimo T, Takizawa A, Serikawa T, et al. Synaptic vesicle glycoprotein 2A (SV2A) regulates kindling epileptogenesis via GABAergic neurotransmission. Sci Rep. 2016;6:27420. https://doi.org/10.1038/srep27420.
7. Sanchez PE, Zhu L, Verret L, Vossel KA, Orr AG, Cirrito JR, et al. Levetiracetam suppresses neuronal network dysfunction and reverses synaptic and cognitive deficits in an Alzheimer's disease model. Proc Natl Acad Sci U S A. 2012;109:E2895.
8. Stockburger C, Miano D, Baeumlisberger M, Pallas T, Arrey TN, Karas M, et al. A mitochondrial role of SV2a protein in aging and Alzheimer's disease: studies with Levetiracetam. J Alzheimers Dis. 2016;50:201–15. https://doi.org/10.3233/JAD-150687.
9. Hou Z, Lei H, Hong S, Sun B, Fang K, Lin X, et al. Functional changes in the frontal cortex in Parkinson's disease using a rat model. J Clin Neurosci. 2010;17:628–33. https://doi.org/10.1016/j.jocn.2009.07.101.
10. Mattheisen M, Muhleisen TW, Strohmaier J, Treutlein J, Nenadic I, Alblas M, et al. Genetic variation at the synaptic vesicle gene SV2A is associated with schizophrenia. Schizophr Res. 2012;141:262–5. https://doi.org/10.1016/j.schres.2012.08.027.
11. Selkoe DJ. Alzheimer's disease is a synaptic failure. Science. 2002;298:789–91. https://doi.org/10.1126/science.1074069.
12. Sperling RA, Aisen PS, Beckett LA, Bennett DA, Craft S, Fagan AM, et al. Toward defining the preclinical stages of Alzheimer's disease: recommendations from the National Institute on Aging-Alzheimer's Association workgroups on diagnostic guidelines for Alzheimer's disease. Alzheimers Dement. 2011;7:280–92. https://doi.org/10.1016/j.jalz.2011.03.003.
13. Estrada S, Lubberink M, Thibblin A, Sprycha M, Buchanan T, Mestdagh N, et al. [^{11}C]UCB-A, a novel PET tracer for synaptic vesicle protein 2A. Nucl Med Biol. 2016;43:325–32. https://doi.org/10.1016/j.nucmedbio.2016.03.004.
14. Warnock GI, Aerts J, Bahri MA, Bretin F, Lemaire C, Giacomelli F, et al. Evaluation of ^{18}F-UCB-H as a novel PET tracer for synaptic vesicle protein 2A in the brain. J Nucl Med. 2014;55:1336–41. https://doi.org/10.2967/jnumed.113.136143.
15. Becker G, Warnier C, Serrano ME, Bahri MA, Mercier J, Lemaire C, et al. Pharmacokinetic characterization of [^{18}F]UCB-H PET radiopharmaceutical in the rat brain. Mol Pharm. 2017;14:2719–25. https://doi.org/10.1021/acs.molpharmaceut.7b00235.
16. Bretin F, Bahri MA, Bernard C, Warnock G, Aerts J, Mestdagh N, et al. Biodistribution and radiation dosimetry for the novel SV2A radiotracer [^{18}F]UCB-H: first-in-human study. Mol Imaging Biol. 2015;17:557–64. https://doi.org/10.1007/s11307-014-0820-6.

17. Bahri MA, Plenevaux A, Aerts J, Bastin C, Becker G, Mercier J, et al. Measuring brain synaptic vesicle protein 2A with positron emission tomography and [^{18}F]UCB-H. Alzheimers Dement (NY). 2017;3:481–6. https://doi.org/10.1016/j.trci.2017.08.004.
18. Mercier J, Archen L, Bollu V, Carre S, Evrard Y, Jnoff E, et al. Discovery of heterocyclic nonacetamide synaptic vesicle protein 2A (SV2A) ligands with single-digit nanomolar potency: opening avenues towards the first SV2A positron emission tomography (PET) ligands. ChemMedChem. 2014;9:693–8. https://doi.org/10.1002/cmdc.201300482.
19. Nabulsi NB, Mercier J, Holden D, Carre S, Najafzadeh S, Vandergeten MC, et al. Synthesis and preclinical evaluation of ^{11}C-UCB-J as a PET tracer for imaging the synaptic vesicle glycoprotein 2A in the brain. J Nucl Med. 2016;57:777–84. https://doi.org/10.2967/jnumed.115.168179.
20. Finnema SJ, Nabulsi NB, Mercier J, Lin SF, Chen MK, Matuskey D, et al. Kinetic evaluation and test-retest reproducibility of [^{11}C]UCB-J, a novel radioligand for positron emission tomography imaging of synaptic vesicle glycoprotein 2A in humans. J Cereb Blood Flow Metab. 2017:271678X17724947. doi:https://doi.org/10.1177/0271678X17724947.
21. Finnema SJ, Nabulsi NB, Eid T, Detyniecki K, Lin SF, Chen MK, et al. Imaging synaptic density in the living human brain. Sci Transl Med. 2016;8:348ra96. https://doi.org/10.1126/scitranslmed.aaf6667.
22. Hong S, Beja-Glasser VF, Nfonoyim BM, Frouin A, Li S, Ramakrishnan S, et al. Complement and microglia mediate early synapse loss in Alzheimer mouse models. Science. 2016;352:712–6. https://doi.org/10.1126/science.aad8373.
23. van Spronsen M, Hoogenraad CC. Synapse pathology in psychiatric and neurologic disease. Curr Neurol Neurosci Rep. 2010;10:207–14. https://doi.org/10.1007/s11910-010-0104-8.
24. Kaufman AC, Salazar SV, Haas LT, Yang J, Kostylev MA, Jeng AT, et al. Fyn inhibition rescues established memory and synapse loss in Alzheimer mice. Ann Neurol. 2015;77:953–71. https://doi.org/10.1002/ana.24394.
25. Haas LT, Salazar SV, Smith LM, Zhao HR, Cox TO, Herber CS, et al. Silent allosteric modulation of mGluR5 maintains glutamate signaling while rescuing Alzheimer's mouse phenotypes. Cell Rep. 2017;20:76–88. https://doi.org/10.1016/j.celrep.2017.06.023.
26. Hilton J, Yokoi F, Dannals RF, Ravert HT, Szabo Z, Wong DF. Column-switching HPLC for the analysis of plasma in PET imaging studies. Nucl Med Biol. 2000;27:627–30.
27. Chen MK, Mecca AP, Naganawa M, Finnema SJ, Toyonaga T, Lin SF, et al. Assessing synaptic density in Alzheimer disease with synaptic vesicle glycoprotein 2A positron emission tomographic imaging. JAMA Neurol. 2018;75:1215–24. https://doi.org/10.1001/jamaneurol.2018.1836.
28. Sandiego CM, Weinzimmer D, Carson RE. Optimization of PET-MR registrations for nonhuman primates using mutual information measures: a multi-transform method (MTM). Neuroimage. 2013;64:571–81. https://doi.org/10.1016/j.neuroimage.2012.08.051.
29. Gunn RN, Gunn SR, Cunningham VJ. Positron emission tomography compartmental models. J Cereb Blood Flow Metab. 2001;21:635–52. https://doi.org/10.1097/00004647-200106000-00002.
30. Innis RB, Cunningham VJ, Delforge J, Fujita M, Gjedde A, Gunn RN, et al. Consensus nomenclature for in vivo imaging of reversibly binding radioligands. J Cereb Blood Flow Metab. 2007;27:1533–9. https://doi.org/10.1038/sj.jcbfm.9600493.
31. Cunningham VJ, Rabiner EA, Slifstein M, Laruelle M, Gunn RN. Measuring drug occupancy in the absence of a reference region: the Lassen plot re-visited. J Cereb Blood Flow Metab. 2010;30:46–50. https://doi.org/10.1038/jcbfm.2009.190.
32. Pike VW, Aigbirhio FI. Reactions of cyclotron-produced [^{18}F]fluoride with diaryliodonium salts-a novel single-step route to no-carrier-added [18]fluoroarenes. J Chem Soc Chem Commun. 1995:2215–6. https://doi.org/10.1039/C39950002215.
33. Rotstein BH, Stephenson NA, Vasdev N, Liang SH. Spirocyclic hypervalent iodine(III)-mediated radiofluorination of non-activated and hindered aromatics. Nat Commun. 2014;5:4365. https://doi.org/10.1038/ncomms5365.
34. Cardinale J, Ermert J, Humpert S, Coenen HH. Iodonium ylides for one-step, no-carrier-added radiofluorination of electron rich arenes, exemplified with 4-(([F-18] fluorophenoxy)-phenylmethyl) piperidine NET and SERT ligands. RSC Adv. 2014;4:17293–9. https://doi.org/10.1039/c4ra00674g.
35. Jin XD, Davies RP. Copper-catalysed aromatic-Finkelstein reactions with amine-based ligand systems. Catal Sci Technol. 2017;7:2110–7. https://doi.org/10.1039/c7cy00538e.
36. Bielawski M, Malmgren J, Pardo LM, Wikmark Y, Olofsson B. One-pot synthesis and applications of N-heteroaryl iodonium salts. Chemistryopen. 2014;3:19–22. https://doi.org/10.1002/open.201300042.
37. Neumann CN, Hooker JM, Ritter T. Concerted nucleophilic aromatic substitution with ^{19}F$^-$ and ^{18}F. Nature. 2016;538:274. https://doi.org/10.1038/nature19311.
38. Makaravage KJ, Brooks AF, Mossine AV, Sanford MS, Scott PJ. Copper-mediated Radiofluorination of Arylstannanes with [^{18}F]KF. Org Lett. 2016. https://doi.org/10.1021/acs.orglett.6b02911.
39. Sanford MS, Scott PJ. Moving metal-mediated ^{18}F-fluorination from concept to clinic. ACS Cent Sci. 2016;2:128–30. https://doi.org/10.1021/acscentsci.6b00061.
40. Sander K, Gendron T, Yiannaki E, Cybulska K, Kalber TL, Lythgoe MF, et al. Sulfonium salts as leaving groups for aromatic labelling of drug-like small molecules with fluorine-18. Sci Rep. 2015;5:9941. https://doi.org/10.1038/srep09941.
41. Tredwell M, Preshlock SM, Taylor NJ, Gruber S, Huiban M, Passchier J, et al. A general copper-mediated nucleophilic ^{18}F fluorination of arenes. Angew Chem Int Ed Engl. 2014;53:7751–5. https://doi.org/10.1002/anie.201404436.
42. Lynch BA, Lambeng N, Nocka K, Kensel-Hammes P, Bajjalieh SM, Matagne A, et al. The synaptic vesicle protein SV2A is the binding site for the antiepileptic drug levetiracetam. P Natl Acad Sci USA. 2004;101:9861–6. https://doi.org/10.1073/pnas.0308208101.
43. Laruelle M, Slifstein M, Huang Y. Relationships between radiotracer properties and image quality in molecular imaging of the brain with positron emission tomography. Mol Imaging Biol. 2003;5:363–75.
44. Cai Z, Li S, Matuskey D, Nabulsi N, Huang Y. PET imaging of synaptic density: a new tool for investigation of neuropsychiatric diseases. Neurosci Lett. 2019;691:44–50. https://doi.org/10.1016/j.neulet.2018.07.038.
45. Li S, Cai Z, Wu X, Holden D, Pracitto R, Kapinos M, et al. Synthesis and in vivo evaluation of a novel PET radiotracer for imaging of synaptic vesicle glycoprotein 2A (SV2A) in nonhuman Primates. ACS Chem Neurosci. 2019;10:1544–54. https://doi.org/10.1021/acschemneuro.8b00526.
46. Constantinescu CC, Tresse C, Zheng M, Gouasmat A, Carroll VM, Mistico L, et al. Development and in vivo preclinical imaging of Fluorine-18-labeled synaptic vesicle protein 2A (SV2A) PET tracers. Mol Imaging Biol. 2018. https://doi.org/10.1007/s11307-018-1260-5.